Homo and Hetero Molecular 3D Nanographenes Employing a Cyclooctatetraene Scaffold

Javier Urieta-Mora,[a,b] *Marcel Krug,*[c] *Wiebke Alex,*[c] *Josefina Perles,*[d] *Israel Fernández,*[a] *Agustín Molina-Ontoria,*[b]* *Dirk M. Guldi,*[c]* *Nazario Martín,*[a,b]*

[a] *Departamento Química Orgánica, Facultad C. C. Químicas, Universidad Complutense de Madrid, Av. Complutense s/n, 28040 Madrid (Spain). Homepage: http://www.ucm.es/info/fullerene/. E-mail: nazmar@ucm.es*

[b] *IMDEA-Nanociencia, C/ Faraday 9, Ciudad Universitaria de Cantoblanco, 28049 Madrid, Spain. E-mail: Agustin.molina@imdea.org*

[c] *Department of Chemistry and Pharmacy Friedrich-Alexander-Universität, Erlangen-Nürnberg, Egerlandstrasse 3, 91058 Erlangen (Germany). E-mail: dirk.guldi@fau.de*

[d] *Single Crystal X-ray Diffraction Laboratory, Interdepartmental Research Service (SIdI), Universidad Autónoma de Madrid Cantoblanco, 28049 Madrid (Spain).*

Abstract

Two novel homo and hetero three-dimensional nanographenes – **NG1** and **NG2** – featuring a cyclooctatetraene core are designed, synthetized, and characterized. A concise and efficient bottom-up methodology was employed during which 24 new carbon-carbon bonds were formed. By means of a Scholl reaction nanographenes with 53 fused rings are realized, which exhibited good solubility in common organic solvents. The resulting saddle-like structures of **NG1** and **NG2** are electron-rich and show good chemical and electrochemical stability. Their molecular structures are fully elucidated by single-crystal X-ray crystallography. From their crystal structure analysis is concluded that both nanographenes are chiral and crystallize as a racemic mixture. Our work was rounded-off by excited state investigations such as electron and energy transfer with electron-acceptors and -donors.

Introduction

Graphene has captured the imagination of researchers due to its groundbreaking chemical and physical properties.[1–4] Owing to its unique electronic properties, graphene is used in many emerging fields such as batteries,[5] organic light-emitting diodes,[6] sensors,[7] and photovoltaic devices,[8–10] just to name a few. Notably, single-layer graphene is a zero band gap semiconductor; a feature, which imposes severe limitations in terms of electronic applications.[11] Opening a band gap in graphene, while retaining its exceptional properties, which is of paramount importance for its use in electronic devices, is a viable strategy to circumvent the aforementioned drawbacks. Band-gap opening in graphene is typically carried out by chemical and/or physical methodologies.[12] The chemical modification of graphene by means of "top-down" approaches alters the lattice of graphene and, as a consequence, not well-defined structures or compositions emerge. In contrast, "bottom-up" approaches using organic synthesis offers a wide palette of tools to precisely control with atomic precision sizes as well as geometries of the resulting "molecular" nanographenes (NGs). Importantly, the latter allows the fabrication of uniform and well-defined molecular structures, which, in contrast to pristine graphene, are strongly fluorescent.

Molecular NGs are compelling choices for molecular electronics,[13] photovoltaic applications,[14] hydrogen storage,[15] and sensing,[16] since their molecular structures can be precisely designed and synthesized to afford related properties on demand.[17] Two main strategies for fabricating molecular NGs, with defined chemical structures, have been developed in recent years. On one hand, oxidative cyclodehydrogenation of custom-made polycyclic aromatic hydrocarbons (PAHs)[18–21] and, on the other hand, on-surface cyclodehydrogenation have evolved into powerful and groundbreaking strategies for the preparation of atomically precise molecular NGs.[22–26] To this end, the 13 fused-benzene rings of hexa-*peri*-hexabenzocoronene (HBC), which are arranged in a 2D disk-shaped fashion, render HBCs the smallest graphene fragment. Driven by its tendency to π-π stacking, highly ordered columnar stacks of HBCs have been exploited for several applications.[20,27–31]

Scheme 1. **Molecular structures of HBC, NG1 and NG2.**

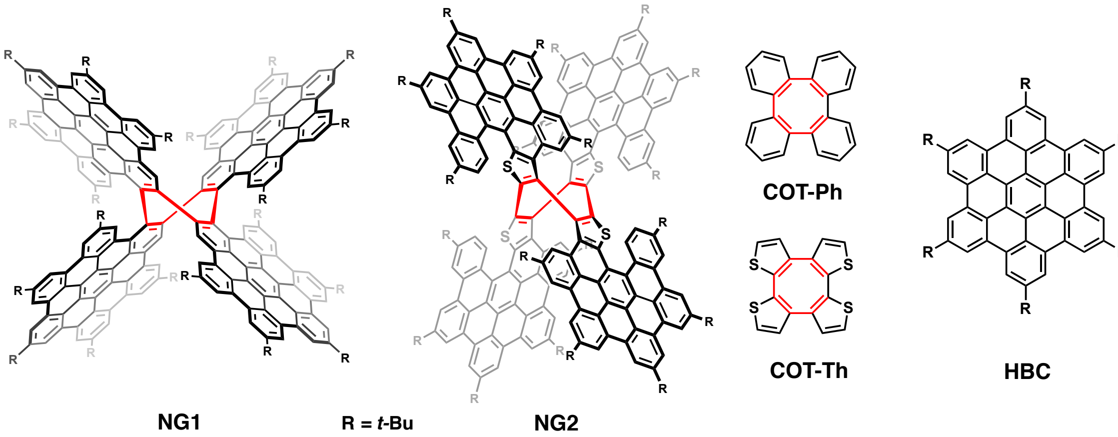

Cyclooctatetraphenylene (COT-Ph) as well as cyclooctatetrathiophene (COT-Th) are π-conjugated scaffolds, whose three-dimensional (3D) geometries are based on their saddle-shape. Four benzenes or thiophenes are *ortho*-annelated, forming a central eight-membered ring. Due to the different symmetry of the C_6 and the C_4S rings, COT-Ph exhibits a D_{2d} symmetry, whereas COT-Th displays a chiral D_2 point group.[32–34] Such unique and non-planar structures are excellent building blocks for the preparation of more sophisticated functional π-conjugated materials and, in turn, further potential applications may be expected.[35–37]

Herein, we describe an efficient “bottom-up” synthesis of two new four-armed, molecular NGs, namely **NG1** and **NG2**, which are based on COT-Ph and COT-Th scaffolds, respectively. **NG1** and **NG2** both are endowed with four HBCs (**Scheme 1**) and feature a fascinating 3-D geometry. The detailed geometrical and structural properties, determined by X-ray analyses, as well as the optical and electrochemical properties of the new molecular NGs, have been rationalized by means of density functional theory (DFT) calculations. Interestingly, the intermolecular excited state interaction between **NG1** and **NG2** were studied in combination with electron accepting materials, such as, tetracyanoethylene and C_{60} and electron donating tetrathiafulvalene.

Results and Discussion

Scheme 2. General synthetic pathway towards (a) homo and (b) hetero, 3D molecular nanographenes.

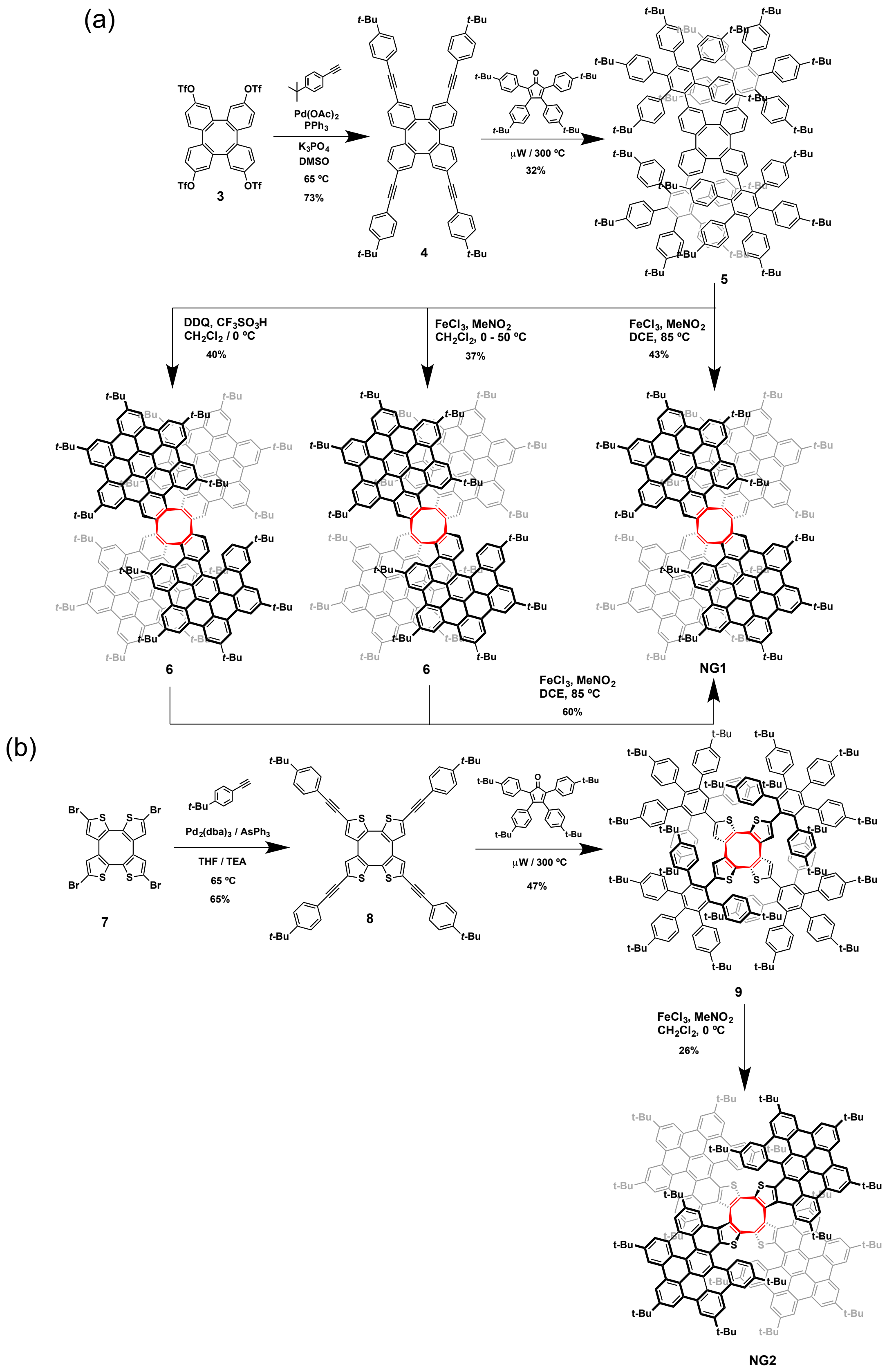

Synthesis. The synthetic routes for the preparation of the molecular NGs were based on stepwise syntheses as illustrated in Scheme 2. Tetraphenylene-2,7,10,15-tetrayl tetrakis(trifluoromethanesulfonate) (**3**), which was prepared in three-steps from 2-iodo-4,4'-dimethoxy-1,1'-biphenyl,[38] was cross-coupled with 4-*tert*-butylphenylacetylene using a palladium-catalyzed Sonogashira reaction to obtain **4**. Microwave-assisted [4+2] cycloaddition of **4** with 2,3,4,5-tetrakis[4-(1,1-dimethylethyl)phenyl]2,4-cyclopentadien-1-one afforded **5**, which, subsequently, underwent intramolecular cyclodehydrogenation mediated by $FeCl_3$ (i.e., Scholl reaction) to generate **6** in moderate yields. Oxidative cyclodehydrogenation at 0 °C generated only 23 new carbon-carbon bonds out of the expected 24 new carbon-carbon bonds and, therefore, the fully coupled **NG1** was not observed. Therefore, we carried out the dehydrogenation reaction under different oxidative coupling conditions, namely trifluoromethanesulfonic acid (TfOH) and 2,3-dichloro-5,6-dicyanobenzoquinone (DDQ), which eventually afforded **6** in relatively good yields. **6** was subjected to a further one-fold $FeCl_3$-mediated oxidative coupling in refluxing dichloroethane to lead to **NG1**. However, gentle heating was needed to yield the complete fusion of all six-membered rings. Under such optimized reaction conditions, **6** was interconverted into the fully coupled **NG1**.

The synthetic strategy for **NG2** is based on the same methodology than that used for the preparation of **NG1**. In particular, 2,5,8,11-tetrabromocycloocta[1,2-*b*:4,3-*b´*:5,6-*b´´*:8,7-*b´´´*]tetrathiophene (**7**), which was prepared from 2,2´-dibromo[3,3´]bithiophene by an oxidative coupling using $CuCl_2$ according to a previously reported method,[35] was subjected to a four-fold palladium-catalyzed Sonogashira reaction with 4-*tert*-butylphenylacetylene. **8** then underwent a microwave-assisted [4+2] cycloaddition with 2,3,4,5-tetrakis[4-(1,1-dimethylethyl)phenyl]2,4-cyclopentadien-1-one to give rise to **9**. Finally, the treatment of the latter species with $FeCl_3$ produced the corresponding fully cyclodehydrogenated molecular **NG2** in moderate yields.

Complete structural characterization of **NG1** and **NG2** plus the corresponding intermediates was conducted by using standard spectroscopic techniques, namely ^1H NMR, ^{13}C NMR, FTIR, and UV−visible (for more details, see the Supporting Information). Mass spectrometry (MALDI-TOF) confirmed the presence of the new molecular **NG1** and

NG2 with molecular ion peaks $[M]^+$ at m/z 3201.7474 (calcd 3201.7523) and 3233.6390 (calcd 3233.6405), respectively.

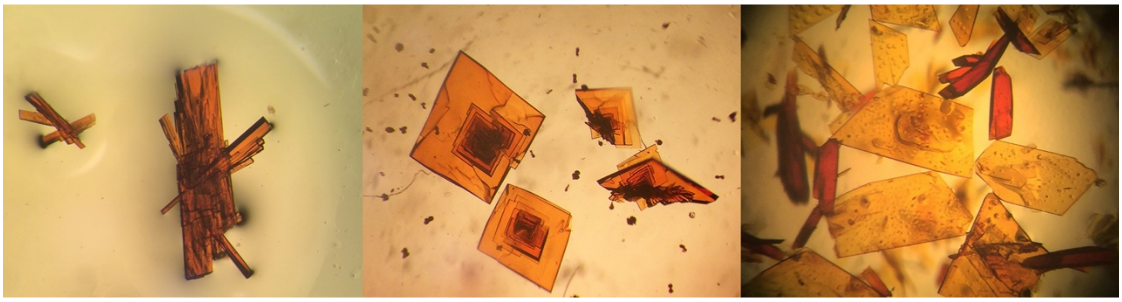

Figure 1. Aggregate of prismatic crystals of **6** (left), laminar crystals of **NG1** (middle), and both prismatic (**2poly**) and laminar (**2plate**) crystals of **NG2** (right).

Single crystal X-ray diffraction. The molecular conformation and crystal packing of **NG1**, **NG2**, and **6** were unequivocally determined by single crystal X-ray diffraction studies. Crystals were obtained by slow diffusion of acetonitrile into their dichloroethane solutions (see Section 4 in the Supporting Information for details). In all cases, the molecular NGs cocrystallize with solvent molecules (dichloroethane and water), which display various degrees of disorder.

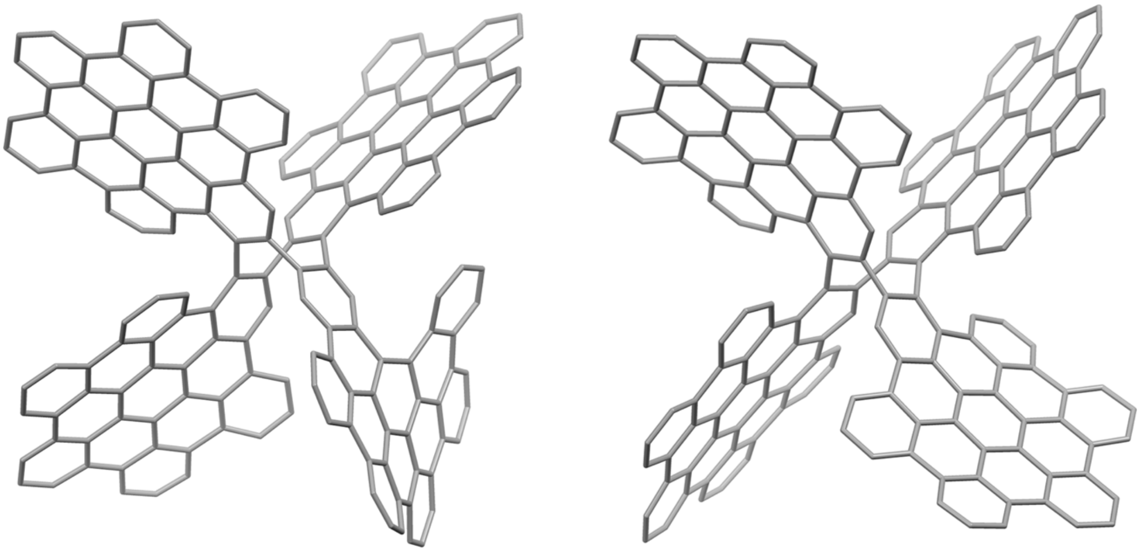

Figure 2. Molecular structures of **6** (left) and **NG1** (right), in which hydrogen atoms and *t*-Bu groups have been omitted for clarity.

The crystals of **6** (see Figure 1, left) appear as aggregates of orange polyhedra. **6** was found to crystallize in the triclinic *P*-1 space group, with a whole molecule in the asymmetric unit, depicted in Figure 2 (left).

The planarity of the four HBCs around the central COT ring was quantified by the dihedral angles between the central ring and the peripheral ones (section S 4.5 in the

SI). The three HBC fragments in **6**, with values ranging from 1.02° to 18.96° are, as expected, more planar than the fourth fragment lacking a C-C bond (16.26 to 27.56°). The molecular packing of **6** is achieved by CH-π interactions, as the bulky peripheral *t*-Bu substituents prevent formation of π-π interactions.

Crystals of **NG1** adopted a laminar morphology (see Figure 1, middle) and the resulting structure is depicted in Figure 2. It crystallizes in the orthorhombic *Pnna* space group with half a molecule in the asymmetric unit.[39] Regarding the planarity of the two crystallographically independent arms, the HBC fragment containing carbon atoms C1-C6, with torsion angles in the range from 7.96° to 16.22°, is considerably less planar than the other one (with values ranging from 3.43° to 10.58°). It is interesting to note that although the COT-Ph saddle-shaped motif is not chiral, **NG1** is chiral due to the disposition of the phenyl rings in the HBC arms around the central 8-membered ring. The arrangement of the HBC arms lowers the initial point symmetry to the resulting chiral D_2 point group as they fail to relate to the mirror planes in D_{2d}.[10] Crystals obtained from the racemic mixture are, however, not enantiopure and contain both isomers in a 50:50 ratio. No close π-π interactions were observed. Instead, the packing is governed by CH-π interactions established by the *t*-butyl substituents. Indeed, the DFT gas-phase optimized structure of a model compound of **NG1**, where the bulky *t*-butyl groups were replaced by methyl groups, confirms the occurrence of the π-π stacking between the HBC groups, which further supports the crucial role of the *t*-butyl groups in preventing close π-π interactions.

On the other hand, two different crystal forms were found for **NG2**: yellow plates (**2plate**) and dark orange polyhedra (**2poly**), as depicted in Figure 1 on the right. Both were isolated and their crystal structures were solved by SCXRD. The polyhedra were extremely difficult to handle, because they lost crystallinity rapidly as soon as they were removed from the mother liquor.

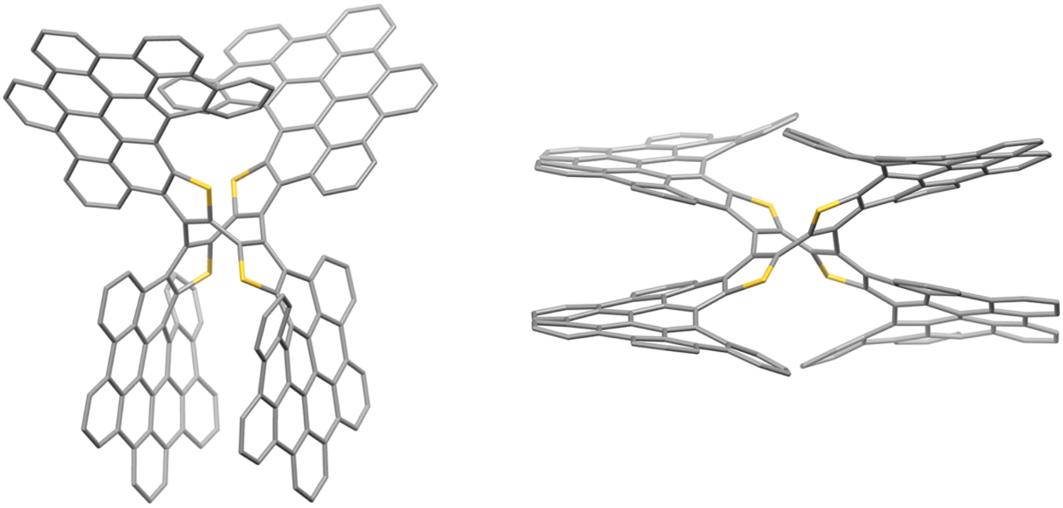

Figure 3. Molecular structures of **2plate** (left) and **2poly** (right), in which hydrogen atoms and *t*-Bu groups have been omitted for clarity.

Crystals of **2plate** and **2poly** crystallize in the triclinic *P*-1 space group, with an entire molecule in the asymmetric unit. **NG2** cocrystallizes with solvent molecules such as dichloroethane or water, from which various degrees of disorder evolve. However, the angles between the HBCs are very different in the two of them (Figure 3). **NG2** in **2poly** displays a more horizontal disposition of the four arms of the central COT, while in **2plate** the substituents are placed in pairs with a V shape. As a matter of fact, they bend to adopt an almost parallel disposition in the case of the fragments containing sulfur atoms S1 and S3, and they trap dichloroethane in between them (Figure S22, left). In **2poly**, we discern similar interactions between two arms and dichloroethane, although dichloroethane is held between the arms of two neighboring **NG2**s (Figure S22, right). Regarding the planarity of the arms, they display similar torsion angles for most of the rings (see table S3.3 and S3.4 in the SI) with maxima of 30.26°, 29.05°, 26.92°, and 30.38° for **2plate** and 28.35°, 30.02°, 28.68°, and 27.27° for **2poly**. As concluded for the crystal structures of **NG1**, the bulky peripheral substituents prevent π-π stacking. The molecular packing in **2plate** and **2poly** is achieved by CH-π interactions, mostly involving dichloroethane in the interstices. **NG2** is chiral, like the core fragment COT-Th, but crystals of **2plate** and **2poly** are both racemic.

The structure of **NG2** was further analyzed by means of Density Functional Theory (DFT) calculations at the B3LYP-D3/def2-SVP level. DFT calculations on models of **2plate** and **2poly**, where the bulky *t*-butyl groups were once again replaced by methyl groups, indicate that both of them are nearly degenerate in the gas-phase with ΔE ≈ 1 kcal/mol (see Computational Details in the Supporting Information). This is fully consistent with the presence of both isomers in the solid-state. In both cases, the sulfur atoms of the thiophenes are placed far from each other to minimize electronic repulsions between their corresponding lone-pairs. In addition, this particular arrangement enables the occurrence of stabilizing intramolecular n–π non-covalent interactions between the lone-pairs of each sulfur and the adjacent aryl groups of the corresponding HBCs. This is visualized in Figure 4.[40]

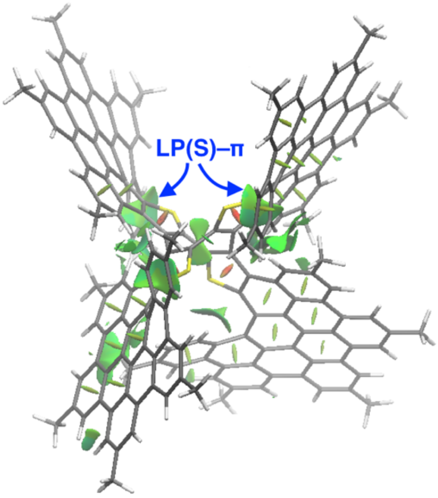

Figure 4. Contour plots of the reduced density gradient isosurfaces (density cutoff of 0.03 a.u.) for **NG2** (**2poly**). The green surfaces indicate attractive non-covalent interactions.

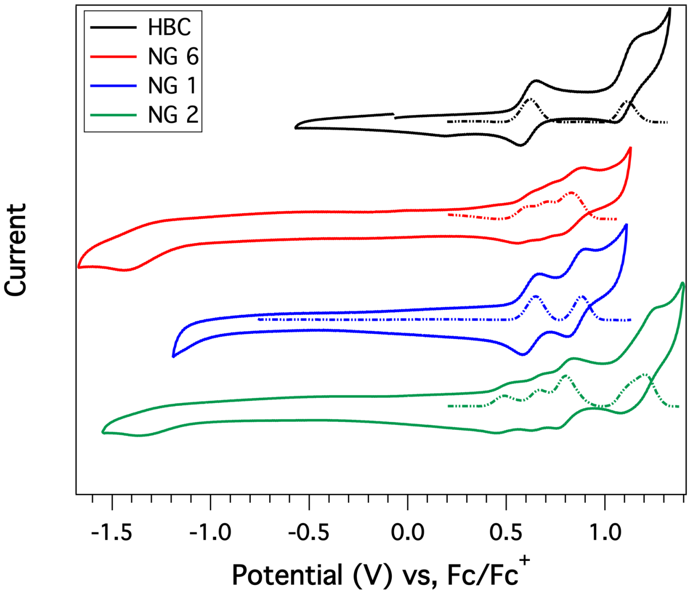

Figure 5. Cyclic voltammograms of **NGs 1** and **2** and the reference NG hexa-*tert*-butylhexa-*peri*-hexabenzocoronene (**HBC**) utilizing 0.1 M $TBAPF_6/CH_2Cl_2$ as the supporting electrolyte and glassy carbon as the working electrode at a scan rate of 100 mV s^{-1}.

Electrochemical Measurements. The electrochemical properties of **NG1**, **NG2**, **6,** and the reference hexa-*tert*-butylhexa-*peri*-hexabenzocoronene (**HBC**) were studied by cyclic voltammetry (CV) and differential pulse voltammetry (DPV) (see Supporting Information for further details). 0.1 M of tetrabutylammonium hexafluorophosphate in dichloromethane was used as supporting electrolyte and a scan rate of 100 mV s^{-1} was applied (Figure 5). The cyclic voltammogram of **NG1** shows two oxidations at +0.62 and +0.85 V *vs. Fc/Fc*$^+$. These oxidations are assigned to two sequential two-electron oxidations, in which a total of four electrons are extracted from the HBCs. The cyclic voltammogram of **NG2** reveals similar features than those seen for the inchoately cyclized form of **NG1.** The first oxidation of **NG2** is, nevertheless, cathodically shifted by 0.14 V relative to **NG1**. This clearly indicates the stronger electron-donating character of **NG2** due to the presence of the thiophenes. The first three reversible oxidations at +0.48, +0.66, and +0.79 V correspond to one-, one-, and two-electron transfers, respectively, and are tentatively assigned to the sequential electron transfer from the thiophene-containing HBCs. The estimated HOMO energies of **NG1**, **NG2**, **6**, and **HBC** are −5.72, −5.58, −5.69, and −5.72 eV, respectively.

Table 1: Electrochemical properties of **NG1**, **NG2**, and reference **HBC**.

Compound	E^1_{ox} [V][a]	E^2_{ox}[V][a]	E^3_{ox} [V][a]	E^4_{ox} [V][a]	E_{HOMO} [eV][b]
HBC	0.62	1.11	-	-	-5.72
6	0.59	0.70	0.82		-5.69
NG1	0.62	0.85	-	-	-5.72
NG2	0.48	0.66	0.79	1.20	-5.58

[a] $E_{1/2}$ determined from CV measurements *vs.* Fc/Fc$^+$. [b] E_{HOMO} is estimated in eV by $E_{HOMO} = -5.1\ \text{eV} - E^{ox}_{1/2}$.

Steady-state absorption and fluorescence assays.

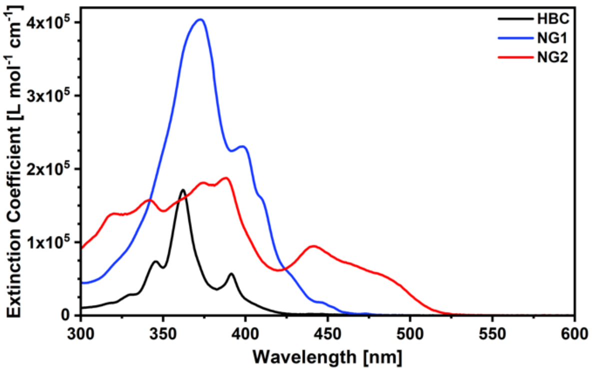

Figure 6. Absorption spectra of **HBC**, **NG1**, and **NG2** in chlorobenzene at room temperature.

We started our spectroscopic investigations of **HBC**, **NG1**, and **NG2** by means of steady-state absorption spectroscopy (Figure 6) in chlorobenzene. The absorption spectrum of **HBC** has characteristic absorption maxima at 329, 345, 362, and 392 nm and two very weak signatures at 439 and 446 nm. In line with the literature,[41–44] we assign the features at 345, 362, and 392 nm to the vibrational fine structure of the symmetry allowed β-transitions, the feature at 329 to the p-bands, and the features at 439 and 446 nm to the α-bands. In principal, p- and α-transitions are symmetry forbidden. H owever, the p-transitions are enabled by mixing with higher lying excited states or symmetry reduction from D_{6h} to D_{3d} through geometric distortions.[43–45]

The absorption spectrum of **NG1** features an absorption maximum at 373 nm with additional fine structure at 398, 410, 429, 437, 447, and 473 nm. In general, the absorption spectrum of **NG1** appears significantly broadened relative to that of **HBC** and the absorption maximum is 11 nm red-shifted. Notably, the absorption of the low-energy α-bands is slightly enhanced, which relates to the loss of symmetry upon substitution. The extinction coefficients of **NG1** are less than four times the corresponding values of **HBC**. For example, a value of 4.03×10^5 L mol^{-1} cm^{-1} at 373 nm should be compared to 1.71×10^5 L mol^{-1} cm^{-1} at 362 nm. Overall, the spectral broadening may contribute to lower extinction coefficients. Broad and overlapping absorption features are noted for **NG2** at 318, 342, 375, 388, 442, and 479 nm. The introduction of thiophenes further reduces the symmetry of the individual moieties, which renders the absorption around 440 nm symmetry allowed.[46]

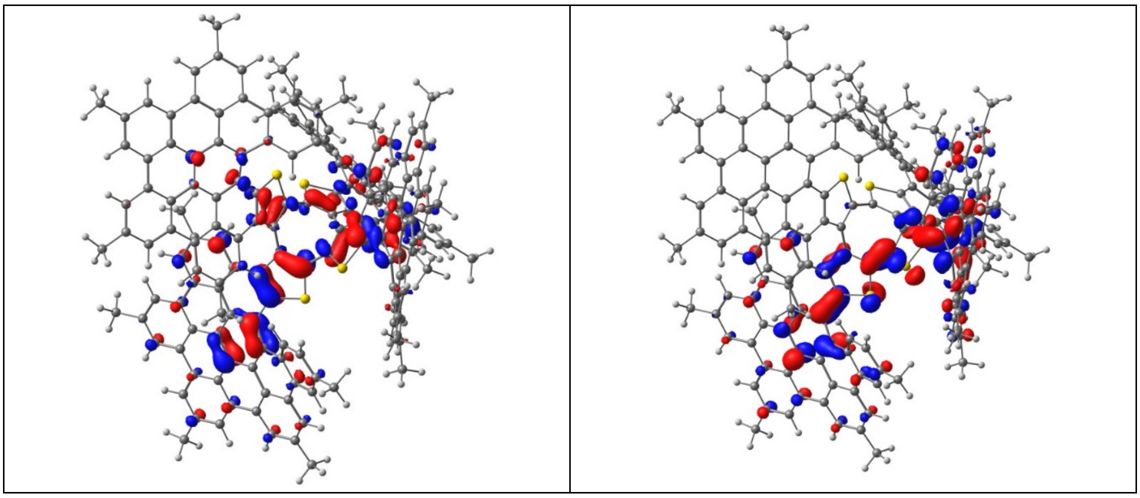

HOMO (−5.19 eV)	LUMO (−2.30 eV)

Figure 7. Computed molecular orbitals involved in the π−π* transitions for **NG2** (isosurface value of 0.05 au) computed at the B3LYP-D3/def2-SVP level.

The observed red-shifted absorption at 479 nm in **NG2** is also very likely due to the involvement of the thiophene moieties. To validate this hypothesis, time-dependent (TD) calculations at the PCM-TD-B3LYP-D3/def2-SVP//B3LYP-D3/def2-SVP level were carried out on the model compound **NG2**. The calculations gave vertical excitation energies at 501 nm, which is in good agreement with the observed experimental value of 479 nm. Such a vertical transition is mainly associated with the promotion of one electron from the HOMO to the LUMO. As depicted in Figure 7, the HOMO should be viewed as a π-molecular orbital, which is not only located on the HBCs but also involves the π-system of the four thiophene fragments. Similarly, the LUMO is a fully delocalized π*-molecular orbital (see Figure 7), which therefore confirms the π-π* nature of the red-shifted absorption at 479 nm.

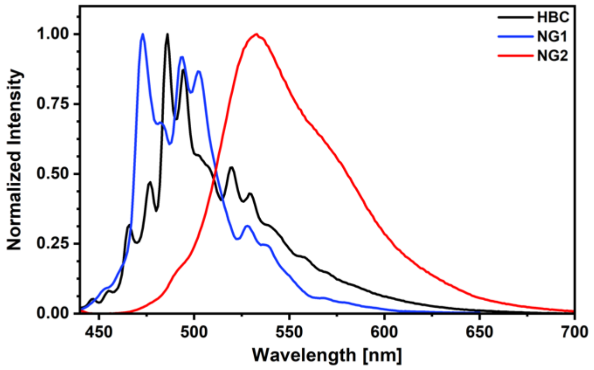

Figure 6. Steady-state fluorescence spectra of **HBC** (λ_{Ex} = 380 nm), **NG1** (λ_{Ex} = 430 nm), and **NG2** (λ_{Ex} = 380 nm) in chlorobenzene at room temperature.

Figure 6 depicts the fluorescence spectra of **HBC**, **NG1**, and **NG2**. Fine structured HBC-centered fluorescence is noted for **NG1** with distinct maxima at 473, 483, 494, 503, 528, and 538 nm. In direct comparison to **HBC**, the fluorescence maxima are red-shifted by around 8 nm. Additionally, the relative intensity of the short-wavelength maximum is significantly enhanced, which is a manifestation of the reduced symmetry of the asymmetrically-substituted HBCs.[41] Any noteworthy fine structure is lost in the fluorescence spectrum of **NG2** and a broad fluorescence maximizing at 533 nm is obtained. We ascribe the loss of the structure to the reduced rigidity and distortions within the molecular plane, as suggested by the crystal structures.

In chlorobenzene, the fluorescence quantum yields of **NG1** and **NG2** are 0.10 and 0.09, respectively, which is about 2.5 times higher than that found for **HBC** with a quantum yield of 0.04 (see Supporting Information for details). A similar trend was also observed for HBC dimers and trimers.[20,21]

Transient Absorption Pump-Probe Experiments

In nanosecond transient absorption pump-probe experiments, we excited **NG1** at 430 nm and probed the deactivation mechanism in Argon-saturated chlorobenzene (Figure S28). Global analysis was based on a two-species kinetic model to fit the raw data. Directly after excitation, we note maxima at 470 and 560 nm together with a broad maximum in the nIR centered at 1139 nm. These singlet-singlet absorptions of **NG1** represent the first species. On a timescale of 30 ns, these features decay and give rise to the second species, which is represented by triplet-triplet absorptions at 509 nm and a broad maximum in the nIR. Overall, the spectroscopic markers of **NG1** are similar to those found for the singlet-singlet/triplet-triplet absorption markers of **HBC**. They are, however, red-shifted and less structured (Figure S27). Therefore, we postulate that both excited states are predominately located on a single HBC rather than delocalized among the four HBCs. The corresponding singlet and triplet excited state lifetimes were determined in the global analysis as 34.5 ns and 302 μs, respectively. As such, the rate constants are 2.6×10^7 s^{-1} for the intersystem crossing (k_{ISC}) and 2.6×10^6 s^{-1} for the radiative ground state recovery (k_F) from the singlet excited state. These are very similar to the corresponding rate constants of **HBC** (Tables S6.1 and S6.2).[47,48] The rate constant of the triplet excited state decay (k_T) is determined as 3.3×10^3 s^{-1}.[49]

Similarly, **NG2** was excited at 460 nm in deaerated chlorobenzene (Figure S29). Again, a two-species kinetic model was used to fit the transient absorption data. The first species is the fast decaying singlet excited state with its singlet-singlet absorption maxima at 531, 679, and 955 nm. To this end, a rapid intersystem crossing yields the triplet excited state, which is the second species, with its absorption maxima at 420 and 538 nm and a broad transient absorption band in the nIR. By means of global analysis, we calculated the singlet excited state lifetime as 0.6 ns and the triplet excited state lifetime as 249 µs, which correspond to rate constants of 1.5 x 10^9 s^{-1} for k_{ISC} and 4.0 x 10^3 s^{-1} for k_T, respectively.[47–49] The significantly faster singlet excited state deactivation stems from an enhanced intersystem-crossing mediated by the heavy atom effect of the sulfur in combination with higher structural flexibility of **NG2** relative to **NG1**.

Additionally, we probed the intermolecular excited state interactions between **HBC**, **NG1**, and **NG2**, on one hand, and electron accepting tetracyanoethylene (TCNE), electron donating tetrathiafulfalene (TTF), and electron accepting fullerene (C_{60}), on the other hand.[50] At first glance, the presence of the aforementioned electron donor and acceptors led, for example, in the case of **NG1** to much shorter triplet excited state lifetimes. By means of concentration dependent assays, in which we varied the electron donor / acceptor concentration from 0 up to 2 x 10^{-3} M, we verified the diffusion-controlled nature of the bimolecular processes.

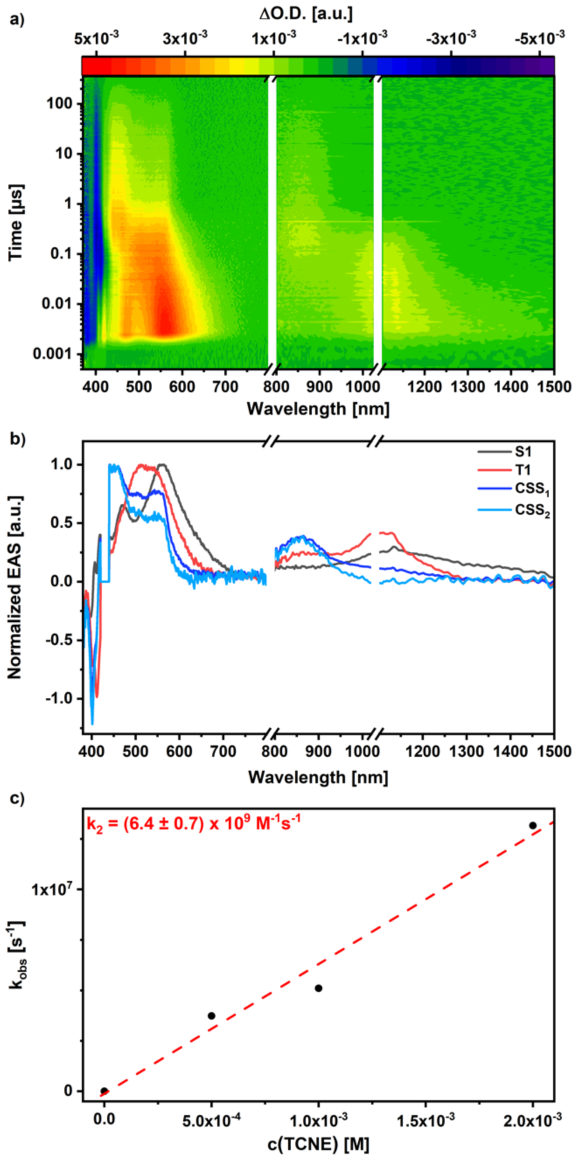

Figure 7. a) Differential transient absorption spectra at time delays between 0 and 350 µs of **NG1** (1×10^{-5} M) with TCNE (1×10^{-3} M) after 430 nm laser excitation (160 nJ) in argon purged PhCl at room temperature. b) EAS obtained by deconvolution of the raw data by means of global analysis. c) Calculation of the bimolecular rate constant k_2 from the triplet excited state lifetime of **NG1** with increasing amounts of TCNE.

A closer look revealed that the presence of TCNE required for the fitting of the transient absorption data, a four-species kinetic model. Relative to **NG1** in the absence of TCNE, the two additional species give rise to similar absorption characteristics at 461, 503, 546, and 865 nm (Figure 7). In the literature, these markers are described as the characteristics of the one-electron oxidized form of **HBC**.[51] Notably, the corresponding 430 nm absorption maximum of the one-electron reduced form of TCNE is masked by the laser excitation. Still, we take our recent observation of a bimolecular electron transfer between photoexcited **HBC** and TCNE,[52] as the basis to postulate an electron transfer from the **NG1** triplet excited state to TCNE.[53] The occurrence of two species with comparable spectroscopic features suggests a common electronic nature and we assign the two transients to states prior (CSS_1) and after diffusional splitting (CSS_2) of the radical ion pair.[54–58] We find rate constants for the diffusive separation in the range from 1.4 to 3.7 x 10^6 s^{-1}.

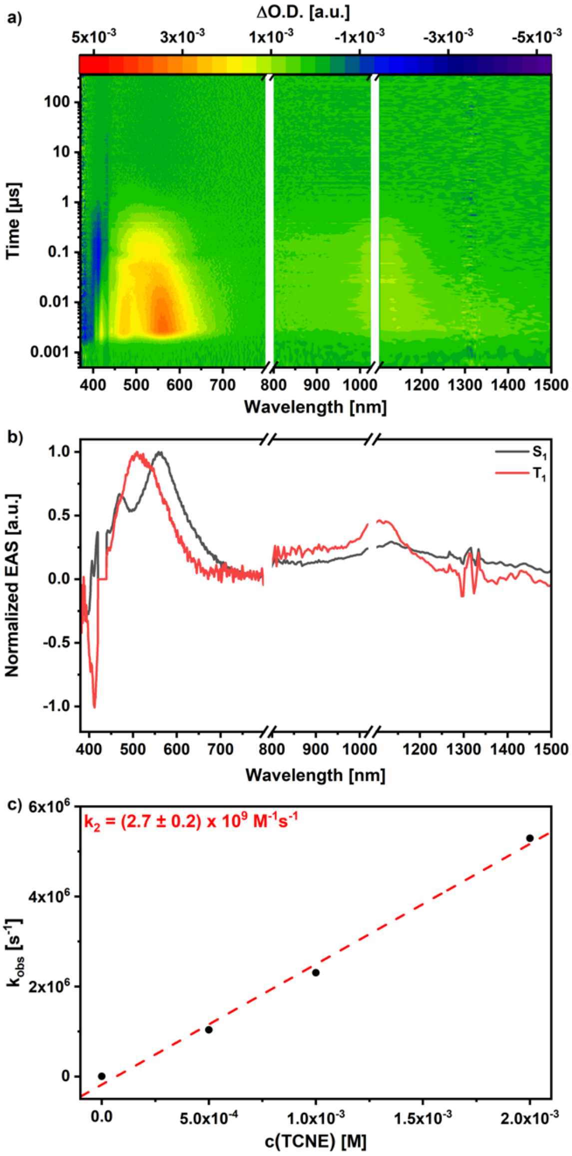

Figure 8. a) Differential transient absorption spectra at time delays between 0 and 350 µs of **NG1** (1 x 10^{-5} M) with TTF (1 x 10^{-3} M) after 430 nm laser excitation (130 nJ) in argon purged PhCl at room temperature. b) EAS obtained by deconvolution of the raw data by means of global analysis. c) Calculation of the bimolecular rate constant k_2 from the triplet excited state lifetime of **NG1** with increasing amounts of TTF.

TTF also quenches the **NG1** triplet excited state, without, however, producing any detectable radical ion pair state characteristics, that is, the one-electron oxidized from of TTF together with the one-electron reduced form of **NG1** (Figure 8). Consequently, the radical ion pair state deactivates faster than its formation and, in turn, is invisible to us in the transient absorption measurements.

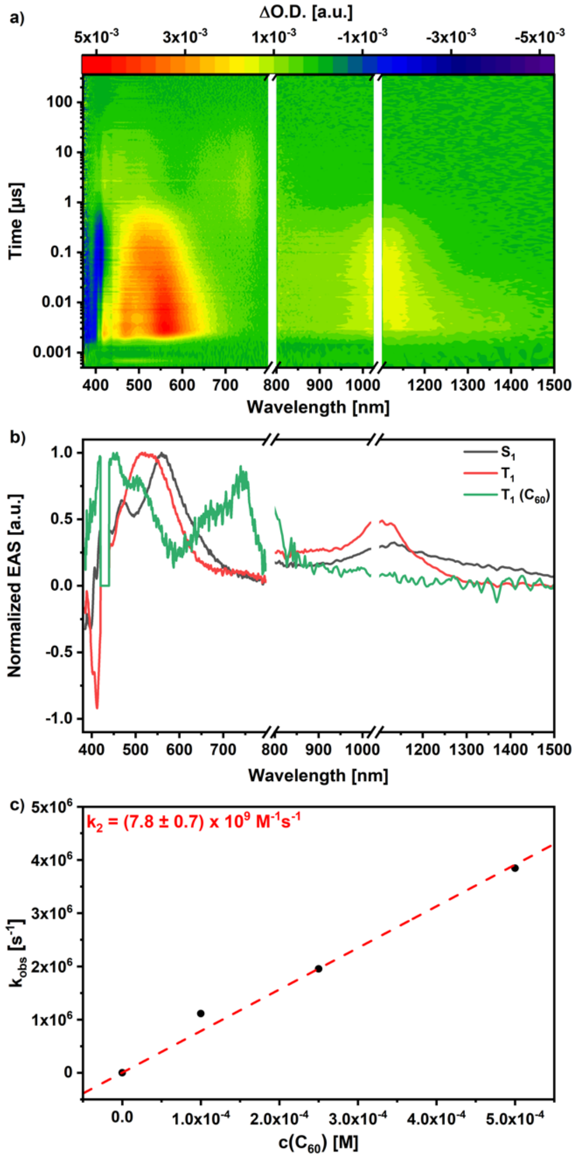

Figure 9. a) Differential transient absorption spectra at time delays between 0 and 350 μs of **NG1** (1 x 10^{-5} M) with C_{60} (2.5 x 10^{-4} M) after 430 nm laser excitation (130 nJ) in argon purged PhCl at room temperature. b) EAS obtained by deconvolution of the raw data by means of global analysis. c) Calculation of the bimolecular rate constant k_2 from the triplet excited state lifetime of **NG1** with increasing amounts of C_{60}.

Finally, we probed the influence of C_{60} on the excited states of **NG1** (**Figure 9**). Here, a three-species kinetic model was necessary to fit the transient absorption data. A concentration dependent quenching of the **NG1** triplet excited state yielded the third species, that is, the triplet excited state of C_{60}. The latter was identified by its characteristic triplet-triplet absorption bands at 452, 508, and 753 nm.[59,60] Accordingly, we conclude a triplet energy transfer from the **NG1** triplet excited state to the ground state of C_{60}.[61]

Table 2. Bimolecular rate constants derived from the concentration dependent quenching of the **NG1/NG2** triplet excited state by TCNE, TTF, and C_{60}.

	TCNE	**TTF**	**C_{60}**
NG1	$(6.4 \pm 0.7) \times 10^9$ M^{-1}	$(2.7 \pm 0.2) \times 10^9$ M^{-1}	$(7.8 \pm 0.7) \times 10^9$ M^{-1}
NG2	-	-	$(7.4 \pm 0.7) \times 10^9$ M^{-1}

To conclude, we probed the excited state dynamics of **NG1** and **NG2** and their excited state interactions with TCNE, TTF, and C_{60}. Table 2 summarizes the bimolecular rate constants, which were derived from concentration dependent assays, and, which are in the range of diffusion controlled processes.[58,62,63] The fact that no electron transfer was observed from **NG2** to TCNE is, however, a surprise, especially considering that **NG2** is a better electron donor than **NG1**. A possible rationale is based on our phosphorescence measurements in frozen MeTHF glass matrices at 80 K (Figures S31-S33). From the latter we derive triplet excited state energies for **NG1** as 2.1 eV and for **NG2** as 1.8 eV.[64] In short, the noticeably lower lying triplet excited state of **NG2** may render the formation of the charge separated state already energetically unfeasible.

Conclusion

In summary, two new homo and hetero saddle-shaped molecular nanographenes (NGs) based on cyclooctatetraene, were successfully synthesized and characterized in depth. Their synthesis allows the formation of 24 new carbon-carbon bonds, increasing the number of annelated rings from five to 53, in just a two-step process, which reflects the efficiency of the bottom-up synthesis. The structures of **NG1** and **NG2** were unambiguously determined by single-crystal X-ray diffraction analyses. As revealed by the SCXRD, the addition of the HBC arms breaks the D_{2d} symmetry of the parent cyclooctatetraene providing π-extended systems with a chiral D_2 point group. Furthermore, **NG2** displays polymorphism and two different crystal forms were found. DFT calculations revealed that the two species found in the **NG2** crystals, that is, **2plate** and **2poly**, were nearly degenerate in the gas-phase with $\Delta E \approx 1$ kcal/mol. This is in sound agreement with the SCXRD studies. Photophysical assays with **NG1** and **NG2** showed that **NG1** undergoes a diffusion controlled photoinduced electron transfer from its triplet excited state in combination with the strong electron-acceptor TCNE, while using C_{60} with a higher LUMO energy /more negative reduction, results in an efficient triplet energy transfer rather than electron transfer. In stark contrast, no electron transfer was observed for **NG2**, while the triplet energy transfer to C_{60} still remained an active deactivation pathway.

Conflicts of interest

There are no conflicts to declare.

Acknowledgments

We thank the Spanish Ministry of Economy and Competitiveness MINECO (projects CTQ2017-83531-R, CTQ2016-78205-P and CTQ2016-81797-REDC, CTQ2016-81911-REDT, CTQ2017-84327-P and Centro de Excelencia Severo Ochoa SEV-2016-0686) and the CAM (QUIMTRONIC, Project Y2018/NMT-4783). J. Perles thanks Dr. Mario Ramírez for his help in the modelling of the disorder in the NGs. This work was also funded by the Deutsche Forschungsgemeinschaft (DFG) via SFB 953 ''Synthetic Carbon Allotropes''.

Notes and references

(1) Dirian, K.; Herranz, M. Á.; Katsukis, G.; Malig, J.; Rodríguez-Pérez, L.; Romero-Nieto, C.; Strauss, V.; Martín, N.; Guldi, D. M. Low Dimensional Nanocarbons—Chemistry and Energy/Electron Transfer Reactions. *Chem. Sci.* **2013**, *4* (12), 4335–4353.

(2) Novoselov, K. S.; Fal'ko, V. I.; Colombo, L.; Gellert, P. R.; Schwab, M. G.; Kim, K. A Roadmap for Graphene. *Nature* **2012**, *490*, 192.

(3) Rodríguez-Pérez, L.; Herranz, M. a Á.; Martín, N. The Chemistry of Pristine Graphene. *Chem. Commun.* **2013**, *49* (36), 3721–3735.

(4) Bottari, G.; Herranz, M. Á.; Wibmer, L.; Volland, M.; Rodríguez-Pérez, L.; Guldi, D. M.; Hirsch, A.; Martín, N.; D'Souza, F.; Torres, T. Chemical Functionalization and Characterization of Graphene-Based Materials. *Chem. Soc. Rev.* **2017**, *46* (15), 4464–4500.

(5) El-Kady, M. F.; Shao, Y.; Kaner, R. B. Graphene for Batteries, Supercapacitors and Beyond. *Nat. Rev. Mater.* **2016**, *1*, 16033.

(6) Li, N.; Oida, S.; Tulevski, G. S.; Han, S.-J. J.; Hannon, J. B.; Sadana, D. K.; Chen, T.-C. C. Efficient and Bright Organic Light-Emitting Diodes on Single-Layer Graphene Electrodes. *Nat. Commun.* **2013**, *4*, 2294.

(7) Dua, V.; Surwade, S. P.; Ammu, S.; Agnihotra, S. R.; Jain, S.; Roberts, K. E.; Park, S.; Ruoff, R. S.; Manohar, S. K. All-Organic Vapor Sensor Using Inkjet-Printed Reduced Graphene Oxide. *Angew. Chemie - Int. Ed.* **2010**, *49* (12), 2154–2157.

(8) Acik, M.; Darling, S. B. Graphene in Perovskite Solar Cells: Device Design, Characterization and Implementation. *J. Mater. Chem. A* **2016**, *4* (17), 6185–6235.

(9) Mahmoudi, T.; Wang, Y.; Hahn, Y.-B. Graphene and Its Derivatives for Solar Cells Application. *Nano Energy* **2018**, *47*, 51–65.

(10) Martín, N. Carbon Nanoforms for Photovoltaics: Myth or Reality? *Adv. Energy Mater.* **2017**, *7* (10), 1601102.

(11) Schwierz, F. Graphene Transistors. *Nat. Nanotechnol.* **2010**, *5*, 487.

(12) Xu, X.; Liu, C.; Sun, Z.; Cao, T.; Zhang, Z.; Wang, E.; Liu, Z.; Liu, K. Interfacial Engineering in Graphene Bandgap. *Chem. Soc. Rev.* **2018**, *47* (9), 3059–3099.

(13) Metzger, R. M. Unimolecular Electronics. *Chem. Rev.* **2015**, *115* (11), 5056–5115.

(14) Cao, J.; Liu, Y. M.; Jing, X.; Yin, J.; Li, J.; Xu, B.; Tan, Y. Z.; Zheng, N. Well-Defined Thiolated Nanographene as Hole-Transporting Material for Efficient and Stable Perovskite Solar Cells. *J Am Chem Soc* **2015**, *137* (34), 10914–10917.

(15) Stein, A.; Wang, Z.; Fierke, M. A. Functionalization of Porous Carbon Materials with Designed Pore Architecture. *Adv. Mater.* **2009**, *21* (3), 265–293.

(16) Krieg, M.; Reicherter, F.; Haiss, P.; Ströbele, M.; Eichele, K.; Treanor, M.-J.; Schaub, R.; Bettinger, H. F. Construction of an Internally B3N3-Doped Nanographene Molecule. *Angew. Chemie Int. Ed.* **2015**, *54* (28), 8284–8286.

(17) Fujii, S.; Enoki, T. Nanographene and Graphene Edges: Electronic Structure and Nanofabrication. *Acc. Chem. Res.* **2013**, *46* (10), 2202–2210.

(18) Evans, P. J.; Ouyang, J.; Favereau, L.; Crassous, J.; Fernández, I.; Perles, J.; Martín, N. Synthesis of a Helical Bilayer Nanographene. *Angew. Chemie Int. Ed.* **2018**, *57* (23), 6774–6779.

(19) Fernández-García, J. M.; Evans, P. J.; Medina Rivero, S.; Fernández, I.; García-Fresnadillo, D.; Perles, J.; Casado, J.; Martín, N. π-Extended Corannulene-Based Nanographenes: Selective Formation of Negative Curvature. *J. Am. Chem. Soc.* **2018**, *140* (49), 17188–17196.

(20) Zhang, C.; Liu, Y.; Xiong, X. Q.; Peng, L. H.; Gan, L.; Chen, C. F.; Xu, H. B. Three-Dimensional Nanographene Based on Triptycene: Synthesis and Its Application in Fluorescence Imaging. *Org. Lett.* **2012**, *14* (23), 5912–5915.

(21) Hu, Y.; Wang, D.; Baumgarten, M.; Schollmeyer, D.; Müllen, K.; Narita, A. Spiro-Fused Bis-Hexa-: Peri -Hexabenzocoronene. *Chem. Commun.* **2018**, *54* (96), 13575–13578.

(22) Zhong, Q.; Hu, Y.; Niu, K.; Zhang, H.; Yang, B.; Ebeling, D.; Tschakert, J.; Cheng, T.; Schirmeisen, A.; Narita, A.; et al. Benzo-Fused Periacenes or Double Helicenes? Different Cyclodehydrogenation Pathways on Surface and in Solution. *J. Am. Chem. Soc.* **2019**, *141* (18), 7399–7406.

(23) Weiss, K.; Beernink, G.; Dötz, F.; Birkner, A.; Müllen, K.; Wöll, C. H. Template-Mediated Synthesis of Polycyclic Aromatic Hydrocarbons: Cyclodehydrogenation and Planarization of a Hexaphenylbenzene Derivative at a Copper Surface. *Angew. Chemie Int. Ed.* **1999**, *38* (24), 3748–3752.

(24) Shen, Q.; Gao, H.-Y.; Fuchs, H. Frontiers of On-Surface Synthesis: From Principles to Applications. *Nano Today* **2017**, *13*, 77–96.

(25) Pinardi, A. L.; Otero-Irurueta, G.; Palacio, I.; Martinez, J. I.; Sanchez-Sanchez, C.; Tello, M.; Rogero, C.; Cossaro, A.; Preobrajenski, A.; Gómez-Lor, B.; et al. Tailored Formation of N-Doped Nanoarchitectures by Diffusion-Controlled on-

Surface (Cyclo)Dehydrogenation of Heteroaromatics. *ACS Nano* **2013**, *7* (4), 3676–3684.

(26) Sánchez-Grande, A.; de la Torre, B.; Santos, J.; Cirera, B.; Lauwaet, K.; Chutora, T.; Edalatmanesh, S.; Mutombo, P.; Rosen, J.; Zbořil, R.; et al. On-Surface Synthesis of Ethynylene-Bridged Anthracene Polymers. *Angew. Chemie Int. Ed.* **2019**, *58* (20), 6559–6563.

(27) Wong, W. W. H.; Ma, C.-Q.; Pisula, W.; Yan, C.; Feng, X.; Jones, D. J.; Müllen, K.; Janssen, R. A. J.; Bäuerle, P.; Holmes, A. B. Self-Assembling Thiophene Dendrimers with a Hexa-Peri-Hexabenzocoronene Core−Synthesis, Characterization and Performance in Bulk Heterojunction Solar Cells. *Chem. Mater.* **2010**, *22* (2), 457–466.

(28) Sui, M.-Y.; Pan, Q. Q.; Yin, H.; Sun, G.-Y.; Geng, Y.; Su, Z.-M. Design of Hexabenzocoronene Derivatives as Non-Fullerene Acceptors in Organic Photovoltaics by Bridging Dimers and Modulating Structural Twists. *Sol. RRL* **2017**, *1* (9), 1700060.

(29) Pisula, W.; Kastler, M.; Wasserfallen, D.; Pakula, T.; Müllen, K. Exceptionally Long-Range Self-Assembly of Hexa-Peri-Hexabenzocoronene with Dove-Tailed Alkyl Substituents. *J. Am. Chem. Soc.* **2004**, *126* (26), 8074–8075.

(30) Qin, J. S.; Yuan, S.; Zhang, L.; Li, B.; Du, D. Y.; Huang, N.; Guan, W.; Drake, H. F.; Pang, J.; Lan, Y. Q.; et al. Creating Well-Defined Hexabenzocoronene in Zirconium Metal-Organic Framework by Postsynthetic Annulation. *J. Am. Chem. Soc.* **2019**, *141* (5), 2054–2060.

(31) Yen, H. J.; Tsai, H.; Zhou, M.; Holby, E. F.; Choudhury, S.; Chen, A.; Adamska, L.; Tretiak, S.; Sanchez, T.; Iyer, S.; et al. Structurally Defined 3D Nanographene Assemblies via Bottom-Up Chemical Synthesis for Highly Efficient Lithium Storage. *Adv. Mater.* **2016**, *28* (46), 10250–10256.

(32) Rapson, W. S.; Shuttleworth, R. G.; van Niekerk, J. N. 89. Benzcyclooctatetraenes. Part III. Diphenylene and Tetraphenylene. *J. Chem. Soc.* **1943**, No. 0, 326–327.

(33) Rajca, A.; Rajca, S. Asymmetric Synthesis of Chiral Tetraphenylenes. *Angew. Chemie Int. Ed.* **2010**, *49* (4), 672–674.

(34) Tian, Y.; Wang, G.; Ma, Z.; Xu, L.; Wang, H. Homochiral Double Helicates Based on Cyclooctatetrathiophene: Chiral Self-Sorting with the Intramolecular S⋯N Interaction. *Chem. – A Eur. J.* **2018**, *24* (60), 15993–15997.

(35) Urieta-Mora, J.; García-Benito, I.; Zimmermann, I.; Aragó, J.; Calbo, J.; Grancini, G.; Molina-Ontoria, A.; Ortí, E.; Martín, N.; Nazeeruddin, M. K. Saddle-like, π-Conjugated, Cyclooctatetrathiophene-Based, Hole-Transporting Material for Perovskite Solar Cells. *J. Mater. Chem. C* **2019**, *7* (22), 6656–6663.

(36) Sun, C. J.; Wang, P. F.; Wang, H.; Han, B. H. All-Thiophene-Based Conjugated Porous Organic Polymers. *Polym. Chem.* **2016**, *7* (31), 5031–5038.

(37) Marsella, M. J. Classic Annulenes, Nonclassical Applications. *Acc. Chem. Res.* **2002**, *35* (11), 944–951.

(38) Zhu, C.; Zhao, Y.; Wang, D.; Sun, W.-Y. Y.; Shi, Z. Palladium-Catalyzed Direct Arylation and Cyclization of o-Iodobiaryls to a Library of Tetraphenylenes. *Sci. Rep.* **2016**, *6* (May), 33131.

(39) The two halves of the molecule are related by a two-fold axis.

(40) Johnson, E. R.; Keinan, S.; Mori-Sánchez, P.; Contreras-García, J.; Cohen, A. J.;

Yang, W. Revealing Noncovalent Interactions. *J. Am. Chem. Soc.* **2010**, *132* (18), 6498–6506.

(41) Hendel, W.; Khan, Z. H.; Schmidt, W. Hexa-Peri-Benzocoronene, a Candidate for the Origin of the Diffuse Interstellar Visible Absorption Bands ? *Tetrahedron* **1986**, *42* (4), 1127–1134.

(42) Rouillé, G.; Steglich, M.; Huisken, F.; Henning, T.; Müllen, K. UV/Visible Spectroscopy of Matrix-Isolated Hexa-Peri-Hexabenzocoronene: Interacting Electronic States and Astrophysical Context. *J. Chem. Phys.* **2009**, *131* (20), 204311.

(43) Rieger, R.; Müllen, K. Forever Young: Polycyclic Aromatic Hydrocarbons as Model Cases for Structural and Optical Studies. *J. Phys. Org. Chem.* **2010**, *23* (4), 315–325.

(44) Fukuda, R.; Ehara, M. Theoretical Study on the Excited Electronic States of Coronene and Its π-Extended Molecules Using the Symmetry-Adapted Cluster-Configuration Interaction Method. *Bull. Chem. Soc. Jpn.* **2013**, *86* (4), 445–451.

(45) Bräuchle, C. Symmetry Distortions and Pseudo-Jahn-Teller Effect of Peri- and Cata-Hexabenzocoronene in Their Triplet States as Obsevered by ODMR Techniques. *Chem. Phys.* **1982**, *67* (1), 97–109.

(46) Any assignment according to Clar’s nomenclature renders impossible due to the bent structure and different symmetry of NG2. See reference 43.

(47) This calculation neglects internal-conversion as a competitive process.

(48) Turro, N. J. *Modern Molecular Photochemistry*; University Science Books: Sausalito, USA, 1991.

(49) We verified the triplet nature by oxygen quenching experiments.

(50) In supplementary steady-state absorption and emission and time resolved femtosecond transient absorption experiments, we found no evidence for ground state interactions or quenching of the nanographenes singlet excited state.

(51) Rathore, R.; Burns, C. L. A Practical One-Pot Synthesis of Soluble Hexa- p Eri-Hexabenzocoronene and Isolation of Its Cation-Radical Salt. *J. Org. Chem.* **2007**, *68* (10), 4071–4074.

(52) Reger, D.; Haines, P.; Heinemann, F. W.; Guldi, D. M.; Jux, N. Helical Structures Oxa [7] Superhelicene : A p -Extended Helical Chromophore Based on Angewandte. *Angew. Chem. Int. Ed.* **2018**, *57*, 5938–5942.

(53) Michiya Itho. Dimerization and Electronic Absorption Spectra of Tetracyanoethylene Anion in Solution and Solid. *Bull. Chem. Soc. Jpn.* **1972**, *45*, 1947–1950.

(54) Gould, I. R.; Ege, D.; Moser, J. E.; Farid, S. Efficiencies of Photoinduced Electron-Transfer Reactions: Role of the Marcus Inverted Region in Return Electron Transfer within Geminate Radical-Ion Pairs. *J. Am. Chem. Soc.* **1990**, *112* (11), 4290–4301.

(55) Gould, I. R.; Young, R. H.; Moody, R. E.; Farid, S. Contact and Solvent-Separated Geminate Radical Ion Pairs in Electron-Transfer Photochemistry. *J. Phys. Chem.* **1991**, *95* (5), 2068–2080.

(56) Kikuchi, K.; Takahashi, Y.; Hoshi, M.; Niwa, T.; Katagiri, T.; Miyashi, T. Free Enthalpy Dependence of Free-Radical Yield of Photoinduced Electron Transfer in Acetonitrile. *J. Phys. Chem.* **1991**, *95* (6), 2378–2381.

(57) Angulo, G.; Rosspeintner, A.; Lang, B.; Vauthey, E. Optical Transient Absorption Experiments Reveal the Failure of Formal Kinetics in Diffusion Assisted Electron Transfer Reactions. *Phys. Chem. Chem. Phys.* **2018**, *20* (39), 25531–25546.
(58) Kavarnos, G. J.; Turro, N. J. Photosensitization by Reversible Electron Transfer: Theories, Experimental Evidence, and Examples. *Chem. Rev.* **1986**, *86* (2), 401–449.
(59) Guldi, D. M.; Prato, M. Excited-State Properties of C 60 Fullerene Derivatives. *Acc. Chem. Res.* **2000**, *33* (10), 695–703.
(60) Arbogast, J. W.; Darmanyan, A. P.; Foote, C. S.; Rubin, Y.; Diederich, F. N.; Alvarez, M. M.; Anz, S. J.; Whetten, R. L. Photophysical Properties of C60. *J. Phys. Chem.* **1991**, *95* (10), 11–12.
(61) Similar experiments were performed with NG2. However, neither the presence of TCNE nor TTF introduced any changes regarding the triplet excited state lifetimes of NG2. The only notable exception is C60. Here, we noticed an efficient triplet energy transfe.
(62) Wilkinson, F.; McGarvey, D. J.; Olea, A. F. Excited Triplet State Interactions with Molecular Oxygen: Influence of Charge Transfer on the Bimolecular Quenching Rate Constants and the Yields of Singlet Oxygen [O*2(1.DELTA.g)] for Substituted Naphthalenes in Various Solvents. *J. Phys. Chem.* **2005**, *98* (14), 3762–3769.
(63) Turró, C.; Zaleski, J. M.; Karabatsos, Y. M.; Nocera, D. G. Bimolecular Electron Transfer in the Marcus Inverted Region. *J. Am. Chem. Soc.* **1996**, *118* (25), 6060–6067.
(64) Note that the energy of NG1 is in the same range than that of HBC with 2.2 eV.

Table of Contents